

COMPUTATIONAL ANALYSIS OF SIZE EFFECT AND FAILURE MODES IN REINFORCED CONCRETE BEAMS

VLADISLAV GUDŽULIĆ* AND GÜNTHER MESCHKE*

*Ruhr University Bochum, Institute for Structural Mechanics
Universitätsstraße 150, 44801 Bochum, Germany
e-mail: vladislav.gudzulic@rub.de, www.sd.rub.de

Key words: Cohesive Zone Model, Reinforced-Concrete Modeling, Size Effect, Failure Modes, Discrete Fracture, Discrete Reinforcement

Abstract. This paper presents a computational approach for simulating the fracture behavior of reinforced concrete. Cracks are discretely modeled using zero-thickness cohesive interface elements, while the reinforcement is explicitly represented by elastoplastic Timoshenko beam elements. The interaction between reinforcement and concrete is captured through specially developed coupling elements. To demonstrate the performance of the proposed computational approach, two series of experiments on reinforced concrete beams without shear reinforcement subjected to four-point bending were numerically analyzed in a 3D setting. In the first series of tests, the SL series performed by Syroka-Korol and Tejchman, the beam size was scaled in two dimensions while the span-to-depth and reinforcement ratios were kept constant. The distinct feature of these tests is that the failure mode was consistent across all sizes, enabling size-effect analysis. In the second series, the S1 series by Suchorzewski et al., only the beam depth was scaled, while the span, load location, and reinforcement ratios remained unchanged. This series exhibited markedly different failure modes for each size, allowing the assessment of the capabilities of the proposed modeling approach to capture the effects of the shape and size on the mechanical response of reinforced concrete beams. The proposed computational approach effectively captures size-dependent peak loads, failure modes, and fracture patterns in all investigated tests.

1 INTRODUCTION

Numerical analyses of structures made of quasi-brittle composite materials such as reinforced concrete require robust models for the opening and propagation of cracks that adequately represent the discontinuous character of the fracture processes and consider stress transfer mechanisms occurring within the fracture process zone. The first numerical approaches for fracture analyses were introduced in the 1960s and 1970s [1, 2]. Over the last 50 years, two major approaches for modeling damage and fracture have been discerned - the discrete and smeared approaches. This paper is concerned

with discrete fracture modeling.

The discrete approaches are modeling cracks as discrete surfaces, with their constitutive behavior defined through traction-separation relations. Hence, no localization limiters are required.

A family of embedded crack methods allows for incorporating strong and weak discontinuities into the finite element kinematics, such as in formulations proposed in [3]. A noteworthy advantage of this class of methods is that they can be formulated to avoid increasing the number of global degrees of freedom. This approach, however, requires a sophisticated finite

element technology, as the standard formulation suffers from various locking issues (see [4]).

The eXtended Finite Element Method (XFEM) [5, 6] enables modeling discrete crack propagation without re-meshing. One difficulty associated with the XFEM method is the need to track the cracks throughout the computational domain, which is quite complex when multiple cracking in 3D is considered, as in structural simulations of reinforced concrete (RC).

The classical discrete approach is the cohesive zone model based on zero-thickness interface elements [7]. In the context of concrete fracture, many models exist, such as [8, 9, 10], to name a few. This approach has a significant advantage in that it can naturally simulate multiple cracking. Nevertheless, it also comes with some disadvantages, such as the high computational cost and the inherent mesh bias because possible crack paths are restricted to paths between the solid finite elements. The issue of computational expense can be mitigated by adaptive interface insertion procedures [11, 12], and in order to reduce the mesh bias, complex re-meshing strategies are sometimes applied (see e.g., [13]), or mesh reorientation schemes [14].

An alternative to the previously described methods are lattice-based and discrete element methods (e.g., [15, 16, 17]). One of the challenges associated with this class of models is that the material parameters, such as Young's modulus, cannot be directly used as input parameters. Rather, the mechanical properties of lattice elements must be calibrated to obtain the matching elastic behavior.

This paper proposes a displacement-based discrete fracture model utilizing zero-thickness interface elements equipped with a cohesive-frictional traction-separation relation that also incorporates a crack dilatancy submodel. Additionally, the paper describes a model for reinforcement bars based on elastoplastic TIMOSHENKO beam elements and the coupling elements that enforce the frictional bonding between concrete and reinforcement.

The performance of the proposed model is

evaluated by numerical analyses of the two sets of experiments on RC beams without shear reinforcement subjected to four-point bending. The first set of experiments by Syroka-Korol and Tejchman [18] involves beams scaled in two dimensions with the span-to-depth and reinforcement ratios constant. The distinct feature of these tests is that the failure mode was consistent across all sizes, enabling size-effect analysis. The second set of experiments by Suchorzewski et al. [19] involves beams whose depth was scaled while the span and reinforcement ratios remained fixed across all sizes. This series exhibited different failure modes for each size. The selected experiments present challenging benchmarks for fracture models as they involve size-effect and size-dependent failure modes in reinforced concrete. Therefore, they enable a thorough assessment of the capabilities of the proposed computational approach to capture the main features of the analyzed fracture experiments.

2 DISCRETE MODELING OF CRACKING BEHAVIOR IN RC

In this work, the concrete bulk is assumed to be a homogeneous linear elastic medium. All nonlinearities are lumped into cohesive cracks. The bulk material is discretized by tetrahedral finite elements with four nodes, while the cracking of the matrix is modeled using cohesive zero-thickness interface elements. The zero-thickness interface elements are adaptively inserted between solid elements according to the algorithm described in [12] and [20]. The interface element kinematics are defined according to the local coordinate system $x'-y'-z'$ illustrated in Figure 1a. The local coordinate x' always points in the direction of the normal to the middle surface of the interface element, and the coordinates y' and z' are mutually orthogonal and lie in the plane of the middle surface. The crack opening in the local coordinate system of the interface element $[[\mathbf{u}']]$ is calculated as

$$[[\mathbf{u}']] = \mathbf{R}\mathbf{N}_u \mathbf{u}^e, \quad (1)$$

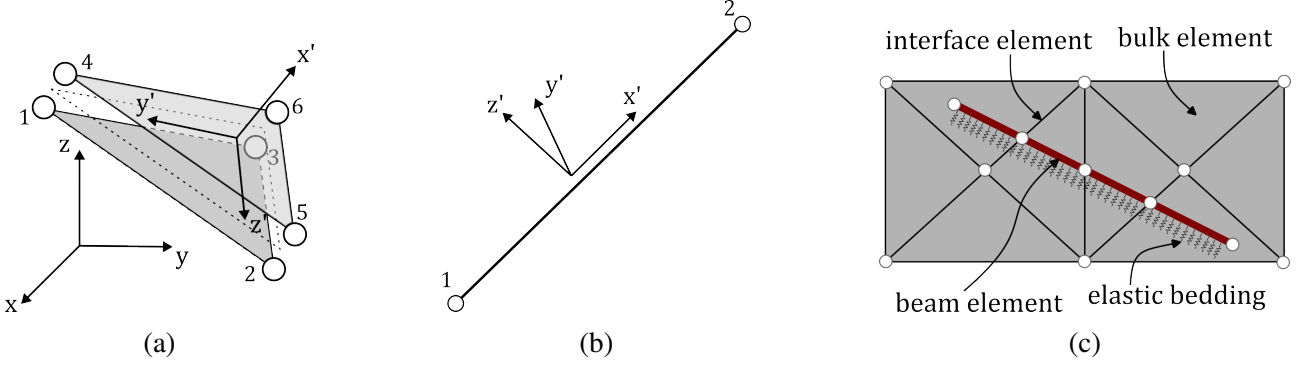


Figure 1: Components of the model for RC structures: (a) zero-thickness interface elements, (b) TIMOSHENKO beam elements, (c) penalty-based frictional coupling between rebar and the background mesh.

where \mathbf{u}^e are the nodal displacements, \mathbf{N}_u is the displacement jump operator, and \mathbf{R} is the rotation matrix (see [21] for details). The expression for the interface element internal force vector ($\mathbf{f}_{\text{int}}^{ie}$) reads:

$$\mathbf{f}_{\text{int}}^{ie} = \iint_{\Gamma_c^e} \mathbf{N}_u^T \mathbf{R}^T \mathbf{t}'_c dA, \quad (2)$$

where Γ_c^e is the surface area of the middle surface, and \mathbf{t}'_c is the traction vector in the local coordinate system of the interface element, described in the following subsection.

The rebars in this work are modeled utilizing beam theory (see, e.g., [22]). The reference (neutral) line of the rebar is discretized in C^0 continuous 1D straight linear TIMOSHENKO beam finite elements (see Figure 1b) with reduced integration. The approximated material strains at any point of the cross-section in the local coordinate system of the beam element are obtained as

$$\boldsymbol{\varepsilon}' = \mathbb{S} \hat{\mathbf{R}} \hat{\mathbf{u}}^e, \quad (3)$$

where $\hat{\mathbf{u}}^e$ are the generalized nodal displacements, the auxiliary matrix \mathbb{S} [22] defined as

$$\mathbb{S} = \begin{bmatrix} 1 & 0 & 0 & 0 & z' & -y' \\ 0 & 1 & 0 & -z' & 0 & 0 \\ 0 & 0 & 1 & y' & 0 & 0 \end{bmatrix}, \quad (4)$$

\mathbf{B} is the discrete gradient operator and $\hat{\mathbf{R}}$ is a 12×12 block rotation matrix (see [21] for details). The kinematic relations presented above

allow for a dimensional reduction of the reinforcement model from 3D to 1D, fully representing rebar kinematics utilizing only its axis. The internal force vector ($\mathbf{f}_{\text{int}}^{be}$) of the beam element can be evaluated as:

$$\mathbf{f}_{\text{int}}^{be} = \int_{L^{be}} \hat{\mathbf{R}}^T \mathbf{B}^T \hat{\boldsymbol{\Sigma}}' dx'. \quad (5)$$

where L^{be} is the beam element length, and $\hat{\boldsymbol{\Sigma}}'$ is the vector of stress resultants evaluated via the integration of the stresses across the beam cross-section as

$$\hat{\boldsymbol{\Sigma}}' = \iint_{A^{be}} \mathbb{S}^T \begin{bmatrix} \sigma_{x'x'} \\ \tau_{x'y'} \\ \tau_{x'z'} \end{bmatrix} dA, \quad (6)$$

with A^{be} denoting the cross-section area of the beam element. It should be noted that the stress resultants defined in Eq. 6 depend only on $\sigma_{x'x'}$, $\tau_{x'y'}$, and $\tau_{x'z'}$ components of the CAUCHY stress tensor in the local coordinate system of the beam cross-section. The remaining components are required to vanish ($\sigma_{y'y'} = \sigma_{z'z'} = \tau_{y'z'} = 0$), which is enforced algorithmically through an iterative procedure proposed in [23].

The coupling between reinforcement and concrete is conceptualized as a penalty-based line element connecting the reinforcement and the background finite element mesh of the bulk material discretized by solid tetrahedral elements, illustrated in Figure 1c. This element is equipped with a cohesive-frictional bond relation and impenetrability constraints that prevent

the reinforcement from freely moving inside the solid elements. The relative slip between rebar and concrete at a specific integration point of the coupling element is evaluated as:

$$[[\mathbf{u}]]'_b = \mathbf{R}(\mathbf{u}_r - \mathbf{u}_c) = \mathbf{R}[\mathbf{N}_r \quad -\mathbf{N}_c] \begin{bmatrix} \hat{\mathbf{u}}_r^e \\ \mathbf{u}_c^e \end{bmatrix}, \quad (7)$$

where $\hat{\mathbf{u}}_r^e$ and \mathbf{u}_c^e denote the nodal displacements of reinforcement and concrete, \mathbf{R} is the rotation matrix, and \mathbf{N}_r and \mathbf{N}_c denote the shape function values of the beam and solid element evaluated at the specific integration point of the coupling element [21]. The local coordinate system is defined such that the local x' coordinate points in the direction of the reinforcement (Figure 1b). Frictional interactions and impenetrability constraints are treated on the level of constitutive relation, where they are coupled with a traction-separation relation that defines the initiation of debonding and constitutive behavior of the bond through the traction vector \mathbf{t}'_b . The internal force vector of the coupling element ($\mathbf{f}_{\text{int}}^{ce}$) can be evaluated as:

$$\mathbf{f}_{\text{int}}^{ce} = \int_{L^{be}} [\mathbf{N}_r \quad -\mathbf{N}_c]^T \mathbf{R}^T \mathbf{t}'_b \pi \phi dx', \quad (8)$$

where L^{be} is the beam element length, and ϕ is the diameter of the rebar.

2.1 Constitutive behavior of concrete

This subsection introduces the traction-separation relation for discrete cracks, describing crack initiation and the evolution of residual strength in plain concrete. It also includes sub-models for crack closure, frictional contact, and dilatancy within the constitutive framework. In this way, all mechanical processes related to cracking are addressed at the material level. Total traction at a single material point can be evaluated as

$$\begin{aligned} \mathbf{t}' = & (1 - d_c) K_c \begin{bmatrix} [[u'_{x'}]] - [[u'_{x'}]]_{\text{dil}} \\ \frac{\beta^2}{\kappa} [[u'_{y'}]] \\ \frac{\beta^2}{\kappa} [[u'_{z'}]] \end{bmatrix} \\ & + d_c K_c \begin{bmatrix} [[u'_{x'}]] - [[u'_{x'}]]_{\text{dil}} \\ [[u'_{y'}]] - [[u'_{y'}]]_{\mu} \\ [[u'_{z'}]] - [[u'_{z'}]]_{\mu} \end{bmatrix} H(-t'_{x'}). \end{aligned} \quad (9)$$

where $[[u'_{x'}]]$, $[[u'_{y'}]]$, and $[[u'_{z'}]]$ are components of the crack opening vector in the local coordinate system of the crack, $[[u'_{x'}]]_{\text{dil}}$ is the normal opening due to dilatancy, $[[u'_{y'}]]_{\mu}$ and $[[u'_{z'}]]_{\mu}$ denote components of frictional sliding vector, d_c is the damage parameter, K_c is the penalty parameter that regularizes the crack initiation, $\beta = f_s/f_t$ is the ratio between shear and tensile strength, $\kappa = G_{F,II}/G_F$ is the ratio between fracture energies in mode II and mode I, and $H(-t'_{x'})$ is the contact activation function (Heaviside function). Contact activation function can be equivalently expressed in terms of the current crack normal opening and the dilatancy contribution so that:

$$H(-([u'_{x'}]] - [[u'_{x'}]]_{\text{dil}})) = \begin{cases} 1, & [[u'_{x'}]] - [[u'_{x'}]]_{\text{dil}} \leq 0, \\ 0, & \text{otherwise} \end{cases} \quad (10)$$

The damage evolution is driven by the maximal value $\alpha_{\text{max}} = \max_{t \in [0, T]}(\alpha_c(t))$ of equivalent crack opening (α_c) experienced by the material point from the beginning of the analysis ($t = 0$) to the current time ($t = T$). The relation for equivalent crack opening (α_c) as proposed in [9]

$$\alpha_c = \sqrt{\langle [[u'_{x'}]] \rangle_+^2 + \frac{\beta^2}{\kappa^2} ([[u'_{y'}]]^2 + [[u'_{z'}]]^2)}, \quad (11)$$

is used, where $\langle \bullet \rangle_+$ denotes the MACAULAY brackets. The traction separation law is completed by the definition of the softening function, which ensures that the appropriate amount of fracture energy is dissipated during the cracking process. Here, the bi-linear softening relation $q_c(\alpha_{\text{max}})$ illustrated in Figure 2a is adopted. The softening function reads

$$q_c(\alpha_{\text{max}}) = \begin{cases} f_t \frac{\alpha_1 - \alpha_{\text{max}}}{\alpha_1 - \alpha_0}, & \alpha_0 \leq \alpha_{\text{max}} \leq \alpha_{\text{int}}, \\ f_{t,\text{int}} \frac{\alpha_{\text{ult}} - \alpha_{\text{max}}}{\alpha_{\text{ult}} - \alpha_{\text{int}}}, & \alpha_{\text{int}} < \alpha_{\text{max}} \leq \alpha_{\text{ult}}, \\ 0, & \alpha_{\text{max}} > \alpha_{\text{ult}}, \end{cases} \quad (12)$$

where $\alpha_0 = \frac{f_t}{K_c}$, and parameters $\alpha_1 = 2G_f/f_t + \alpha_0$, $\alpha_{\text{int}} = \alpha_1 - (\alpha_1 - \alpha_0)f_{t,\text{int}}/f_t$ and $\alpha_{c,\text{ult}} = 2G_{f,\text{res}}/f_{t,\text{int}} + \alpha_{\text{int}}$. For concrete it is typically assumed that $f_{t,\text{int}} = 0.25f_t$ and $G_F = G_f + G_{f,\text{res}} = 2G_f$ to $2.5G_f$ (see, e.g., [24]).

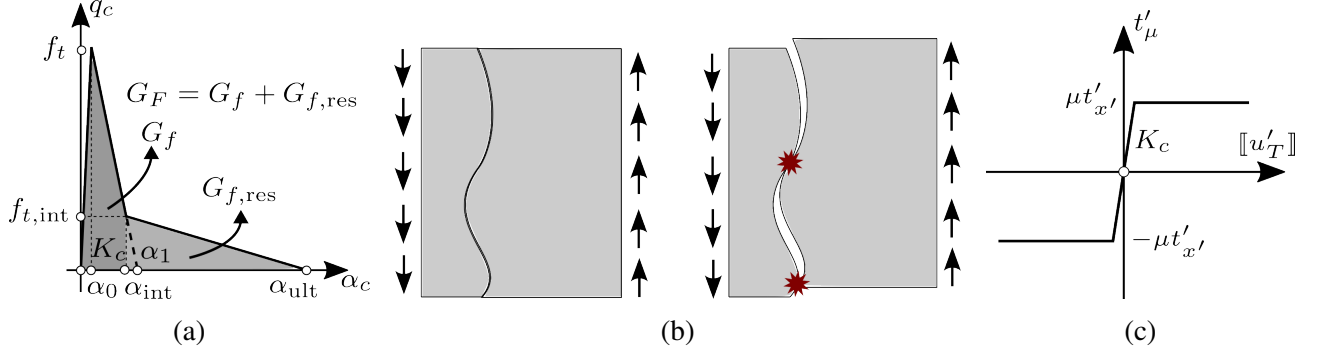


Figure 2: Components of the constitutive model: (a) bilinear softening law describing the progressive loss of cohesion in concrete cracks, (b) crack dilatancy mechanism causing normal opening due to contacts between asperities (indicated by red stars) during tangential sliding, and (c) penalty-regularized elastoplastic model for frictional sliding.

The damage parameter is evaluated as $d_c = \min(1 - \frac{q_c}{K_c \alpha_{\max}}, 1)$. Figure 2b illustrates a simplified physical intuition of the dilatancy stemming from the crack roughness, depicting how shear displacement of crack faces is impeded by asperities in the form of aggregates or crack irregularities. The tangential displacement of crack faces leads to contact between asperities at small crack openings, causing further normal opening of the crack. If reinforcement is present, this mechanism can result in the development of normal compressive forces, thereby increasing frictional resistance. Following the argument by Alfaiate and Sluys [25], this work adopts a total format for expressing dilatancy. The simplified model proposed here defines normal crack opening due to dilatancy ($\llbracket u'_{x'} \rrbracket_{\text{dil}}$) as:

$$\llbracket u'_{x'} \rrbracket_{\text{dil}} = \bar{u}_{\text{dil}} \tanh \left(\frac{\tan(\psi_{\text{dil}})}{\bar{u}_{\text{dil}}} \sqrt{\llbracket u'_{y'} \rrbracket^2 + \llbracket u'_{z'} \rrbracket^2} \right). \quad (13)$$

The hyperbolic tangent function is chosen as a regularization for the bi-linear ramp function. In Eq. 13 ψ_{dil} is a dilatancy angle, \bar{u}_{dil} represents the limit normal opening jump due to dilatancy. According to [26], the value of dilatancy limit \bar{u}_{dil} should be chosen as half the size of the largest aggregate used in a concrete mix.

Frictional sliding between crack faces can occur when cracks are closed and experience compressive and shear stresses. Since frictional sliding can only occur in already initi-

ated cracks, the damage parameter d_c is utilized to distinguish the fraction of cohesive zone that has been fully cracked (see Eq. 9), following the idea proposed in [27]. Friction is modeled using the plasticity framework with penalty parameter K_c to regularize the transition between sticking and slipping states, as illustrated in Figure 2c. Utilizing the elastoplastic analogy, the frictional yield function (f_μ) is defined as:

$$f_\mu(\mathbf{t}'_\mu) = \|\mathbf{t}'_\mu\| - \mu \|\langle -t'_{x'} \rangle_+\| \leq 0, \quad (14)$$

where μ is the COULOMB friction coefficient and $t'_{x'}$ is the normal compressive traction between the crack faces, and \mathbf{t}'_μ is the frictional traction vector. The plastic potential and the corresponding non-associative flow rule are chosen as

$$g_\mu(\mathbf{t}'_\mu) = \|\mathbf{t}'_\mu\|, \quad \llbracket \dot{\mathbf{u}}' \rrbracket_\mu = \dot{\lambda}_\mu \frac{\partial g_\mu}{\partial \mathbf{t}'_\mu}, \quad (15)$$

in order not to produce any dilatant plastic opening in the direction normal to the crack surface (x') since the dilatancy is treated separately. In Eq. 15, $\dot{\lambda}_\mu$ is the plastic multiplier. The friction submodel is completed with KARUSH-KUHN-TUCKER conditions $\dot{\lambda}_\mu \geq 0$, $f_\mu \leq 0$, $\dot{\lambda}_\mu f_\mu = 0$.

2.2 Constitutive behavior of reinforcement

This section briefly outlines the constitutive model for steel rebars modeled as TIMOSHENKO beam elements. During crack-bridging action, reinforcement can be exposed

to considerable stress levels, causing the material behavior to cease being elastic. In this work, the plastification is modeled utilizing an elastic-perfectly plastic Von-Mises law. In particular, the rebars following the TIMOSHENKO beam kinematics obey a 3D constitutive law at the cross-section level. The material strains are calculated on the cross-section level utilizing Eq. 3, and then the stresses are calculated and integrated to obtain the stress resultants in the local coordinate system of the beam according to Eq. 6. In this way, the partial or complete plastification of the cross-section can be distinguished. The elastic part of the material response is characterized by two elasticity parameters (bulk modulus K and shear modulus G), and the plastic part is characterized by the yield stress (σ_y). The yield function (f_y) is defined as:

$$f_y = \sqrt{\frac{3}{2} \boldsymbol{\sigma}'_{dev} : \boldsymbol{\sigma}'_{dev}} - \sigma_y \leq 0, \quad (16)$$

where $\boldsymbol{\sigma}'_{dev} = \boldsymbol{\sigma}' - \frac{1}{3} \text{tr}(\boldsymbol{\sigma}') \mathbf{I}$ is the deviatoric part of the CAUCHY stress tensor $\boldsymbol{\sigma}'$. The associative flow rule is assumed, and so the evolution of plastic strains ($\dot{\boldsymbol{\epsilon}}'_p$) and the strain-like internal variable (α) are defined as

$$\dot{\boldsymbol{\epsilon}}'_p = \dot{\lambda} \frac{\partial f_y(\boldsymbol{\sigma}', \alpha)}{\partial \boldsymbol{\sigma}'}, \quad \dot{\alpha} = \sqrt{\frac{2}{3}} \dot{\lambda}, \quad (17)$$

with $\dot{\lambda}$ being the plastic slip multiplier. The elastoplastic constitutive relation is completed with KARUSH-KUHN-TUCKER conditions, given as $\dot{\lambda} \geq 0$, $f_y \leq 0$, $\dot{\lambda} f_y = 0$.

As mentioned earlier, the stress components $\sigma'_{y'y'}$, $\sigma'_{z'z'}$, and $\tau'_{y'z'}$ are required to vanish due to the modeling assumptions of the beam theory.

2.3 Cohesive-frictional bond model

This subsection introduces the formulation of the cohesive-frictional behavior of the bond between rebar and concrete. The bond between reinforcement and concrete is conceptualized as elastic bedding between the matrix and reinforcement phases. The elastic bedding consists of three distributed springs, oriented to

align with the local coordinate system of the beam. One spring, aligned parallel to the rebar, is equipped with an elastoplastic bond-slip relation, while the two lateral springs have high initial elastic stiffness (penalty parameter K_b) that ensures no lateral penetration of the rebar into the matrix occurs.

The debonding and subsequent frictional slip are modeled utilizing the penalty-regularized elastoplastic framework. The constitutive relation describing the debonding process is defined by the following yield function

$$f_b = |t'_{b,x'}| - q_b(\bar{s}_p) \leq 0, \quad (18)$$

where $t'_{b,x'}$ is the axial bond stress, and $q_b(\bar{s}_p)$ is the stress-like internal variable depending on the accumulated plastic slip \bar{s}_p . The evolution of the bond strength during progressive debonding is adopted from the fib Model Code 2010 [28] in a slightly modified form as:

$$q_b(\bar{s}_p) = \begin{cases} \tau_0, & \bar{s}_p \leq s_0 \\ \Delta\tau_1 \left(\frac{\bar{s}_p}{s_1}\right)^n + \tau_0 + \mu_{sc} p, & s_0 < \bar{s}_p \leq s_1 \\ \tau_{\max} + \mu_{sc} p, & s_1 < \bar{s}_p \leq s_2 \\ \Delta\tau_2 \frac{s_3 - \bar{s}_p}{s_3 - s_2} + \tau_f + \mu_{sc} p, & s_2 < \bar{s}_p \leq s_3 \\ \tau_f + \mu p, & \bar{s}_p > s_3, \end{cases} \quad (19)$$

with $\Delta\tau_1 = \tau_{\max} - \tau_0$ and $\Delta\tau_2 = \tau_{\max} - \tau_f$. In Eq. 19, also illustrated in Figure 3, τ_{\max} , and τ_f describe the maximal and residual bond strengths, while τ_0 denotes the onset of nonlinearity. In this relation, friction is accounted for through $\mu_{sc} p$, where $p = \sqrt{t_{y',b}^2 + t_{z',b}^2}$ is the lateral pressure that rebar exerts on concrete, and μ_{sc} is the COULOMB coefficient between rebar and concrete. The steepness of the segments is controlled through parameters $s_0 = \frac{\tau_0}{K_b}$, s_1 , s_2 , and s_3 . Parameters τ_{\max} , τ_f , s_1 , s_2 , and s_3 can be identified through empirical equations in Model Code [28]. Finally, n is the power-law exponent, adopted as 0.5 in this work.

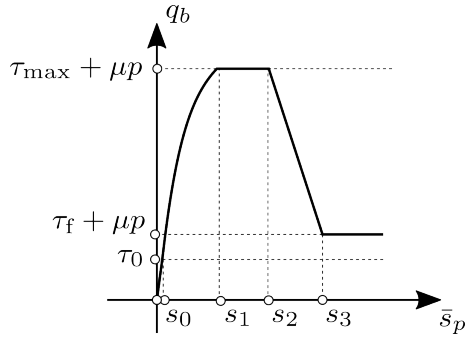


Figure 3: Illustration of the bond-slip law with the interpretation of model parameters.

The evolution of the plastic slip (s_p) and the accumulated plastic slip (\bar{s}_p) are defined as

$$\dot{s}_p = \dot{\lambda}_b \frac{\partial f_b}{\partial t'_{b,x'}}, \quad \dot{\bar{s}}_p = \dot{\lambda}_b, \quad (20)$$

with $\dot{\lambda}_b$ being the plastic slip multiplier. The elastoplastic bond-slip relation is completed with KARUSH-KUHN-TUCKER conditions, given as $\dot{\lambda}_b \geq 0$, $f_b \leq 0$, $\dot{\lambda}_b f_b = 0$.

This completes a brief outline of constitutive models proposed in this work to describe the cracking behavior of reinforced concrete. Further details, including the discretization and implementation aspects, can be found in [21].

3 ANALYSIS OF RC BEAMS

To demonstrate the performance of the proposed discrete fracture modeling approach, two series of experimental size effect tests on reinforced concrete beams subjected to four-point bending performed by Tejchman and coworkers were numerically analyzed in a 3D setting.

3.1 SL series: Constant span-to-depth ratio

In the experimental campaign by [18], beams of three different sizes were investigated. Figure 4 illustrates the four-point bending setup with beam dimensions and locations of supports and loading plates.

The fracture properties of concrete used in the numerical simulations were determined according to recommendations provided by Model Code 2010 [28] utilizing the experimental measurements in [19]. The lower bound of

the characteristic tensile strength was adopted in the numerical analyses ($f_t = 0.7f_{t,m} \approx 2.2\text{MPa}$). The mixed mode fracture parameters ($\beta, \kappa, \mu, \psi_{\text{dil}}$) were adopted according to typical values taken from the literature. All beams were reinforced with ribbed longitudinal reinforcement bars with a reinforcement ratio of 1% (see cross-sections in Figure 4b for rebar placement and diameters). The material properties of steel rebars in the numerical simulations were selected according to the data provided by [18]. Accordingly, Young's modulus was $E_s = 200\text{GPa}$, Poisson's ratio was $\nu = 0.3$, and the yield strength was $\sigma_y = 500\text{MPa}$. The bond parameters for the bond model in the numerical simulations were adopted from [29]. A friction coefficient between steel and concrete of $\mu_{sc} = 0.4$ was assumed. Table 1 provides the complete list of bond properties used in the numerical analyses of the SL beam series. Figure 5a shows comparisons between experimentally and computationally obtained responses for beams of SL series, as well as comparison with numerically obtained responses by Syroka-Korol, Tejchman, and Mroz [29] who used a non-local damage-plasticity approach. The numerically obtained load-displacement curves closely resemble the experimental curves in terms of characteristic features. The calculated peak loads match the experimental peak loads satisfactorily, with only the peak load of the smallest beam slightly overestimated but still within a range of 10% deviation from the mean peak load of the experiments. The failure modes and fracture patterns are very well captured for all sizes, as shown in Figure 5b. In Figure 5b, only the localized cracks are shown, i.e., the interface elements with an opening magnitude greater than 0.075mm. For the smallest beam, the dominant diagonal crack is located slightly closer to the support than in the experiment (more to the left), while the locations of critical diagonal cracks for medium and large beams are captured very well. Compared to the experiments and the modeling approach in [29], the present model shows slightly less abrupt failure, which can be a consequence of the choice of the

Table 1: Material and numerical parameters used in numerical analysis of SL beam series.

Concrete Properties			Concrete-Rebar Bond Properties		
Property	Unit	Value	Property	Unit	Value
E	[MPa]	34000.0	K_b	[N/mm ³]	80000.0
K_c	[N/mm ³]	34000000.0	τ_0	[MPa]	1.0
ν	[-]	0.2	τ_{\max}	[MPa]	11.83
f_t	[MPa]	2.2	τ_f	[MPa]	1.77
$\beta = \frac{f_s}{f_t}$	[-]	2.0	s_1	[mm]	0.6
G_F	[N/mm]	0.14	s_2	[mm]	0.6
$\kappa = \frac{G_{F,II}}{G_F}$	[-]	10.0	s_3	[mm]	1.0
μ	[-]	0.7	μ_{sc}	[-]	0.4
$f_{t,int} = 0.25f_t$	[MPa]	0.55			
$G_f = 0.4G_F$	[N/mm]	0.056			
$\tan \psi_{dil}$	[-]	0.2			
\bar{u}_{dil}	[mm]	16.0			

fib bond-slip model that does not account for the evolution of the radial stresses in the vicinity of the rebar, as discussed in [29]. Nevertheless, the failure occurs by the formation of the dominant shear crack, indicating that the model correctly captures the failure mode.

3.2 S1 series: Varying span-to-depth ratio

This subsection presents the computational investigations of the second set of beams subjected to displacement-controlled four-point bending, the S1 series [19]. Figure 6 illustrates the four-point bending setup with beam dimensions and the locations of supports and loading plates. The experimental data show that the collapse was triggered by a different failure mode for each beam size. These experiments serve as a valuable validation data set to test the capa-

bilities of the developed model to capture different, size-dependent failure modes. The material properties for concrete were adopted according to experimental tests performed in [19] and are provided in Table 2. As in the SL series, the lower bound of the characteristic tensile strength was adopted in the numerical analyses ($f_t = 0.7f_{t,m} \approx 2\text{MPa}$). The mixed-mode fracture parameters were adopted according to the typical values from the literature. The number of ribbed longitudinal rebars used in the experiments varied for different beam sizes to keep the reinforcement ratio of 1.4% constant for all tests. The details about the geometrical properties and placement of rebars are contained in Figure 6. The material properties of steel rebars in numerical simulations were selected according to the data provided in [19]. Accordingly,

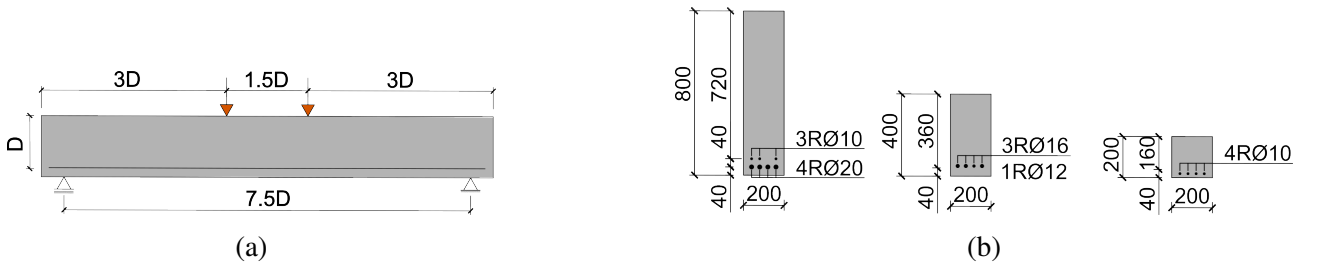


Figure 4: Test setup for the SL beam series: (a) beam dimensions parameterized by the effective section depth $D=\{160,360,750\}$ mm, (b) cross-section dimensions. All dimensions in [mm].

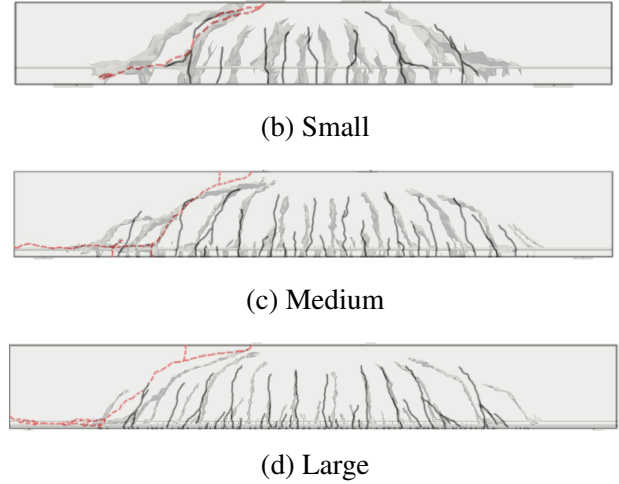
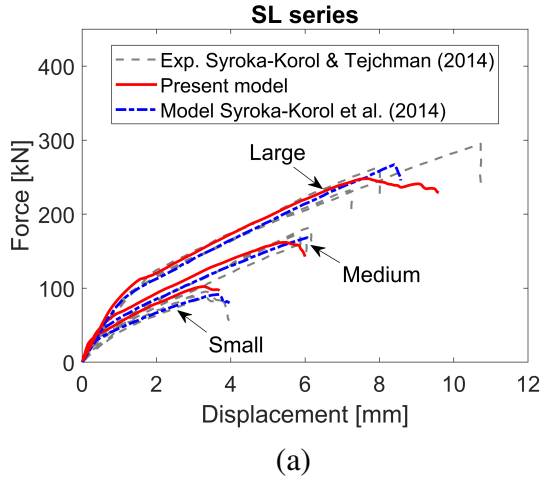


Figure 5: Comparison of experimentally and numerically obtained (a) force-displacement curves for SL beam series for all three sizes, and final experimental and numerical fracture patterns, overlaid for comparison: (b) small, (c) medium, (d) large. Experimental crack patterns reproduced from [18]. Beams in figures are rescaled to the same size.

Young's modulus was $E_s = 205\text{GPa}$, Poisson's ratio was $\nu = 0.3$, and the yield strength was $\sigma_y = 560\text{MPa}$. The bond parameters adopted for numerical simulations are calculated according to recommendations of Model Code 2010 [28], assuming unconfined concrete and good bond conditions. The friction coefficient between steel and concrete was assumed as $\mu_{sc} = 0.4$. Table 2 provides the complete list of bond properties used in numerical analyses of the S1 beam series.

Figure 7a shows comparisons between experimentally and numerically obtained load-displacement curves for three beams of different sizes from the S1 test series, as well as the comparison with numerical results from [30], who used a non-local damage-plasticity model for concrete. Each of the three beams failed under a different failure modes, leading to markedly different load-displacement responses regarding peak loads and ductility. Overall, the calculated response resembles the experimental load-displacement curves well. Also, importantly, the model has shown the capability to capture failure modes and crack patterns correctly for beams of all sizes as shown in Figure 7b (only cracks with opening larger than 0.07mm are shown).

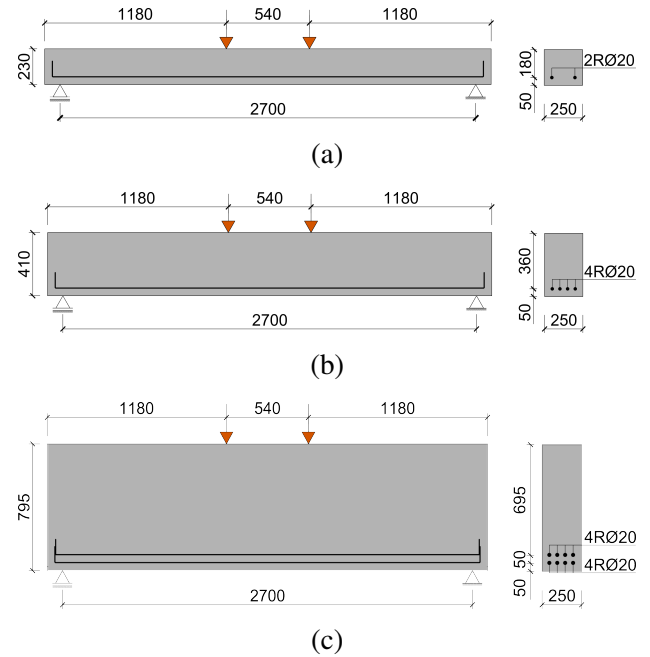


Figure 6: Test setup and dimensions for the S1 beam series: (a) small size beam, (b) medium size beam, and (c) large size beam. All dimensions in [mm].

There are, however, some deviations between experimental and calculated load-displacement curves. In particular, the numerical response of the largest beam shows a stiffer post-cracking response as compared to the experiments.

Table 2: Material and numerical parameters used in numerical analysis of S1 beam series.

Concrete Properties			Concrete-Rebar Bond Properties		
Property	Unit	Value	Property	Unit	Value
E	[MPa]	33100.0	K_b	[N/mm ³]	80000.0
K_c	[N/mm ³]	33100000.0	τ_0	[MPa]	1.0
ν	[-]	0.2	τ_{\max}	[MPa]	16.77
f_t	[MPa]	2.0	τ_f	[MPa]	6.15
$\beta = \frac{f_s}{f_t}$	[-]	4.5	s_1	[mm]	1.0
G_F	[N/mm]	0.1	s_2	[mm]	2.0
$\kappa = \frac{G_{F,II}}{G_F}$	[-]	12.5	s_3	[mm]	10.0
μ	[-]	0.7	μ_{sc}	[-]	0.4
$f_{t,int} = 0.25f_t$	[MPa]	0.5			
$G_f = 0.4G_F$	[N/mm]	0.04			
$\tan \psi_{dil}$	[-]	0.4			
\bar{u}_{dil}	[mm]	8.0			

4 CONCLUSIONS

This paper proposed discrete fracture and reinforcement models and demonstrated their capabilities in simulating bending and shear failure of RC beams subjected to four-point bending tested in two series of size-effect experiments. The model successfully captured the ultimate loads, failure modes, and fracture patterns for all investigated beams. Some deviations in the post-cracking ascending branch observed in the analysis of the largest beam from one set of experiments still need to be further investigated. The sensitivity of the proposed model to individual parameters will be discussed in detail in a forthcoming publication. However, the model has demonstrated its capability to reproduce the different failure modes and crack patterns in all structural experiments, which makes it a suitable tool for both serviceability and failure analysis of RC structures.

5 ACKNOWLEDGMENTS

This research showcases computational models developed within the German Research Foundation (DFG) Priority Program 2020, Cyclic Deterioration of High-Performance Concrete in an Experimental-Virtual Lab (Project 353819637) and the DFG-NSFC collaborative research grant program "Multiscale

Tests, Simulation, Optimization and 3D Printing of UHPFRC Materials and Structures" (Project M-0172). The financial support from the DFG and the National Science Foundation of China (NSFC) is gratefully acknowledged.

REFERENCES

- [1] D. Ngo and A. C. Scordelis. Finite element analysis of reinforced concrete beams. *ACI Journal Proceedings*, 64:152–163, 1967.
- [2] A. Hillerborg, M. Modeer, and P. E. Petersson. Analysis of crack formation and crack growth in concrete by means of fracture mechanics and finite elements. *Cement and Concrete Research*, 6:773–782, 1976.
- [3] Y. Sun, E. Roubin, J. Shao, and J. P. Colliat. Meso-scale Finite Element modeling of the Fracture Process Zone evolution for concrete. *Theoretical and Applied Fracture Mechanics*, 125:103869, 2023.
- [4] J. Oliver, I. F. Dias, and A. E. Huepe. Crack-path field and strain-injection techniques in computational modeling of propagating material failure. *Computer*

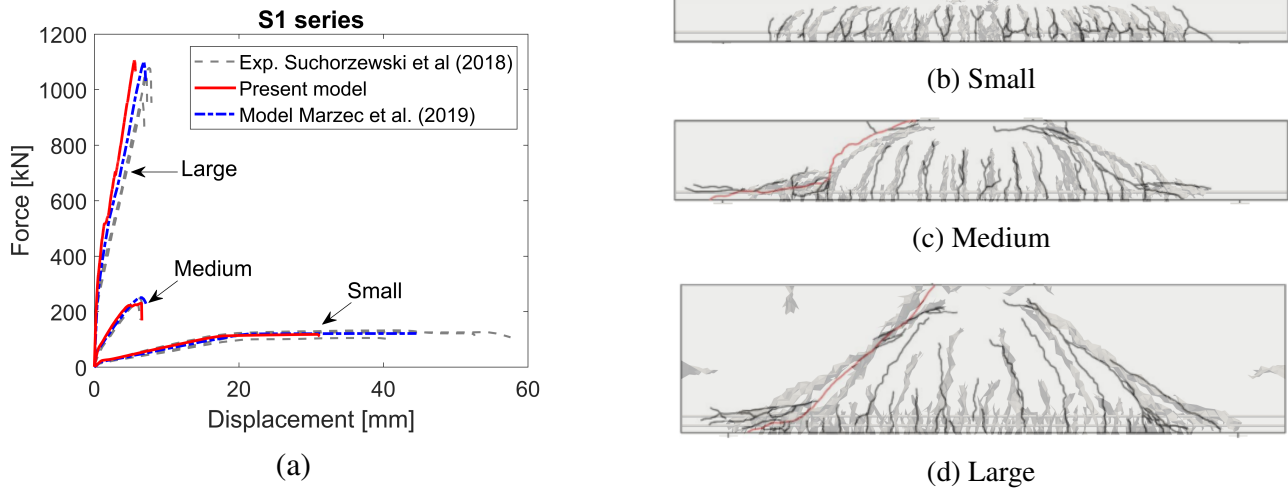


Figure 7: Comparison of experimentally and numerically obtained (a) force-displacement curves for S1 beam series for all three sizes, and final fracture patterns, overlaid for comparison: (b) small, (c) medium, (d) large. Experimental crack patterns reproduced from [19].

Methods in Applied Mechanics and Engineering, 274:289–348, 2014.

- [5] N. Moës and T. Belytschko. Extended finite element method for cohesive crack growth. *Engineering Fracture Mechanics*, 69(7):813–833, 2002.
- [6] G. Meschke, P. Dumstorff, W. Fleming, and S. Jox. Numerical analysis of crack propagation in concrete structures using X-FEM. In G. Meschke, R. de Borst, H. A. Mang, and N. Bicanic, editors, *Computational modeling of concrete structures (EURO-C 2006)*, pages 157–166, 2006.
- [7] M. Ortiz and A. Pandolfi. Finite-deformation irreversible cohesive elements for three-dimensional crack-propagation analysis. *International Journal for Numerical Methods in Engineering*, 44(9):1267–1282, 1999.
- [8] A. Caballero, K. J. Willam, and I. Carol. Consistent tangent formulation for 3D interface modeling of cracking/fracture in quasi-brittle materials. *Computer Methods in Applied Mechanics and Engineering*, 197(33-40):2804–2822, 2008.
- [9] L. Snozzi and J. F. Molinari. A cohesive element model for mixed mode loading with frictional contact capability. *International Journal for Numerical Methods in Engineering*, 93(5):510–526, 2013.
- [10] V. Gudžulić, K. Daadouch, and G. Meschke. Modeling of damage processes in concrete under monotonic and cyclic loading. In *Proceedings of the 11th International Conference on Fracture Mechanics of Concrete and Concrete Structures*, 2023.
- [11] A. Pandolfi and M. Ortiz. An efficient adaptive procedure for three-dimensional fragmentation simulations. *Engineering Computations*, 18(2):148–159, 2002.
- [12] G. H. Paulino, W. Celes, R. Espinha, and Z. J. Zhang. A general topology-based framework for adaptive insertion of cohesive elements in finite element meshes. *Engineering with Computers*, 24(1):59–78, 2008.
- [13] P. O. Bouchard, F. Bay, and Y. Chastel. Numerical modelling of crack propagation: automatic remeshing and comparison of different criteria. *Computer Meth-*

- ods in Applied Mechanics and Engineering*, 192:3887–3908, 2003.
- [14] L. Crusat, I. Carol, and D. Garolera. Application of configurational mechanics to crack propagation in quasi-brittle materials. *Engineering Fracture Mechanics*, 241:107349, 2021.
- [15] J. Eliáš, M. Vořechovský, J. Skoček, and Z. P. Bažant. Stochastic discrete meso-scale simulations of concrete fracture: Comparison to experimental data. *Engineering Fracture Mechanics*, 135:1–16, 2015.
- [16] H. Zhang, B. Šavija, S. C. Figueiredo, and E. Schlangen. Experimentally validated multi-scale modelling scheme of deformation and fracture of cement paste. *Cement and Concrete Research*, 102:175–186, 2017.
- [17] G. Cusatis, D. Pelessone, and A. Men-carelli. Lattice discrete particle model (LDPM) for failure behavior of concrete.I: Theory. *Cement and Concrete Composites*, 33(9):881–890, 2011.
- [18] E. Syroka-Korol and J. Tejchman. Experimental investigations of size effect in reinforced concrete beams failing by shear. *Engineering Structures*, 58:63–78, 2014.
- [19] J. Suchorzewski, E. Korol, J. Tejchman, and Z. Mróz. Experimental study of shear strength and failure mechanisms in RC beams scaled along height or length. *Engineering Structures*, 157:203–223, 2018.
- [20] K. Daadouch. Adaptive Insertion of Cohesive Interface Elements - Application to efficient macro- and mesoscale simulations of concrete cracking. Master’s thesis, Ruhr-University Bochum, 2021.
- [21] V. Gudžulić. *Virtual lab for mechanical testing of steel and steel-fiber reinforced concrete*. Doctoral thesis, Ruhr-Universität Bochum, Universitätsbibliothek, 2024.
- [22] E. Oñate. *Structural analysis with the finite element method. Linear statics: volume 2: beams, plates and shells*. Springer Science & Business Media, 2013.
- [23] S. Klinkel and S. Govindjee. Using finite strain 3d-material models in beam and shell elements. *Engineering Computations*, 19(8):902–921, 2002.
- [24] G. Cusatis and E. A. Schaufert. Cohesive crack analysis of size effect. *Engineering Fracture Mechanics*, 76(14):2163–2173, 2009.
- [25] J. Alfaiate and L. J. Sluys. On the modeling of mixed-mode discrete fracture: Part II–Inclusion of dilatancy. *Engineering Fracture Mechanics*, 182:245–264, 2017.
- [26] P. H. Feenstra, R. de Borst, and J. G. Rots. Numerical study on crack dilatancy part I: models and stability analysis. *Journal of engineering mechanics*, 117(4):733–753, 1991.
- [27] F. Parrinello, B. Failla, and G. Borino. Cohesive-frictional interface constitutive model. *International Journal of Solids and Structures*, 46(13):2680–2692, 2009.
- [28] International Federation for Structural Concrete (fib). *fib Model Code for Concrete Structures 2010*. Ernst & Sohn, 2013.
- [29] E. Syroka-Korol, J. Tejchman, and Z. Mróz. FE analysis of size effects in reinforced concrete beams without shear reinforcement based on stochastic elasto-plasticity with non-local softening. *Finite Elements in Analysis and Design*, 88:25–41, 2014.
- [30] I. Marzec, J. Tejchman, and Z. Mróz. Numerical analysis of size effect in RC beams scaled along height or length using elasto-plastic-damage model enhanced by non-local softening. *Finite Elements in Analysis and Design*, 157:1–20, 2019.